Geophysical Research Letters

RESEARCH LETTER
10.1029/2019GL083148

Dynamic Wedge Failure and Along-Arc Variations of Tsunamigenesis in the Japan Trench Margin

Shuo Ma[1] and **Shiying Nie**[1]

[1]Department of Geological Sciences, San Diego State University, San Diego, CA, USA

Key Points:
- Inelastic wedge deformation can induce large seafloor uplift efficiently landward from trench and diminish near-trench slip on the fault
- Along-arc variation of sediment thickness in the Japan Trench margin can lead to important along-arc variations of tsunamigenesis
- The large tsunami heights along the Sanriku coast in the 2011 Tohoku earthquake can be due to inelastic wedge deformation

Supporting Information:
- Supporting Information S1
- Movie S1

Correspondence to:
S. Ma,
sma@mail.sdsu.edu

Citation:
Ma, S., & Nie, S. (2019). Dynamic wedge failure and along-arc variations of tsunamigenesis in the Japan Trench margin. *Geophysical Research Letters*, *46*. https://doi.org/10.1029/2019GL083148

Received 3 APR 2019
Accepted 25 JUL 2019
Accepted article online 30 JUL 2019

Abstract Elastic dislocation models require large near-trench slip to explain large tsunamigenesis, which is probably best exemplified in the 2011 M9 Tohoku earthquake. However, it is puzzling that the largest Tohoku tsunami heights occurred about 100 km north of the largest slip zone, where bathymetric surveys indicate no large slip at the trench or submarine landslides. Here we show that coseismic yielding of plentiful sediments in the northern Japan Trench margin can induce large inelastic uplift landward from the trench and diminish slip near the trench. The scarcity of sediments in the south leads to nearly elastic response with large slip at the trench and mostly horizontal seafloor displacement. Thus, the variations of sediments along the Japan Trench and sediment yielding can explain the puzzling variations of tsunamigenesis and near-trench slip in this earthquake. Inelastic wedge deformation can be an important mechanism of tsunamigenesis in accretionary and other sediment-filled plate margins.

Plain Language Summary The general consensus about the devastating 2011 Tohoku tsunami is that it was due to large slip at the trench. This can be somewhat misleading because the largest tsunami heights occurred about 100 km north of where the largest trench slip occurred. Using elastic dislocation theory, inversions of tsunami data require large trench slip ~30 m in the north (north of 39°N). However, the bathymetry data before and after the earthquake suggest no large trench slip or submarine landslides in the north. Here we present a mechanism that involves the yielding of sediments in the overriding wedge. Our inelastic wedge deformation model can explain the puzzling observations of large tsunami heights along the Sanriku coast in the north with no or small trench slip and small tsunami in the south with large trench slip. The amount of sediments in a subduction margin can be very important in evaluating tsunami hazard.

1. Introduction

One puzzle about the tsunami generated by the 2011 M9.0 Tohoku earthquake is that the largest tsunami heights occurred in the Sanriku coast, which is about 100 km north of where the largest slip occurred at the trench (Mori et al., 2011). The tsunami runup along the rugged Sanriku coast, up to nearly 40 m, is about 2–3 times larger than the south, causing immense devastation. Most slip models inverted from seismic and geodetic data resolve slip 50 m or larger at the trench updip from the hypocenter (Lay, 2018; Sun et al., 2017, and references therein), supported by bathymetry data before and after the earthquake (Fujiwara et al., 2011). These slip models, based on seismic and/or geodetic data alone, however, resolve little slip north of 39°N (Lay, 2018), which cannot explain the large tsunami heights along the Sanriku coast, even when high-resolution near-shore bathymetry and topography are used in the runup calculations (e.g., Tappin et al., 2014; Yamazaki et al., 2018).

In order to explain the large tsunami heights in the north, near-trench slip as large as ~30 m is required north of 39°N from inversions of tsunami data (e.g., Satake et al., 2013; Yamazaki et al., 2018). However, two profiles of bathymetry data before and after the earthquake north of 39°N indicate no large slip or submarine landslides at the trench (Fujiwara et al., 2017). These findings conflict with the existing tsunami-based inverse slip models and also a submarine landslide model (Tappin et al., 2014). Without large trench slip or submarine landslides, what caused the devastating tsunami along the Sanriku coast? Also, what gave rise to the variations of near-trench slip from south to north?

An important characteristic of the Japan Trench margin is that the amount of the sediments increases systematically from south to north (see Figure 17 of Tsuru et al., 2002, and supporting information Figure S1). South of 38°N, sediments subduct along the plate interface in thin sedimentary channels. However,

sediments north of 38°N increase dramatically to form large sedimentary wedges up to 30–40 km wide and 10–15 km deep in the overriding plate. These large sedimentary wedges directly face the Sanriku coast to the west. Sediments, due to their low shear strength, can fail easily under dynamic stress change during an earthquake. In this work, we will show that it is the inelastic deformation of wedge sediments (wedge failure) that may have caused the devastating tsunami along the Sanriku coast, not large near-trench slip as required by elastic dislocation models. The tsunami heights along the Sanriku coast for both the 2011 Tohoku earthquake and the 1896 Sanriku tsunami earthquake (Kanamori, 1972) were very similar (e.g., Lay, 2018; Satake et al., 2013) suggesting that both devastating tsunami were likely due to the failure of wedge sediments.

In an elastic dislocation model, large slip at the trench on a shallow dipping fault causes mostly horizontal seafloor displacement. When the seafloor is not flat, the horizontal displacement of seafloor slope also leads to certain uplift of ocean, thus contributing to tsunami generation (Tanioka & Satake, 1996). This contribution, however, can be inefficient because seafloor slope landward from the trench is generally small. In the Japan Trench, the seafloor slope landward from the trench is about 6° and 10° along the bathymetry profile(s) in the south (Fujiwara et al., 2011) and north (Fujiwara et al., 2017), respectively. Large earthquake-generated tsunami generally require more efficient seafloor uplift.

Seno (2000) and Tanioka and Seno (2001) first proposed the concept of sediment failure in contributing to seafloor uplift. Ma (2012) and Ma and Hirakawa (2013) modeled inelastic wedge deformation in two-dimensional dynamic rupture models. They showed that for a nearly critical wedge (e.g., Dahlen, 1984; Wang & Hu, 2006), coseismic wedge failure is more efficient in generating seafloor uplift than slip on a shallow dipping fault. With significant inelastic wedge deformation, large uplift can occur landward from the trench with little slip at the trench. Elastic dislocation models with buried slip can also generate peak seafloor uplift landward from the trench, but the uplift is much smaller than that from inelastic wedge deformation given the same seismic moment. The higher efficiency of generating uplift from inelastic deformation (irrespective of wedge criticality) can be understood by considering frictional sliding on conjugate Coulomb microfractures with steeper dips. Inelastic deformation is also a large energy sink (Ma & Hirakawa, 2013), which can lead to the slow rupture velocity, deficiency of high-frequency radiation, and low moment-scaled radiated energy, anomalously observed for shallow subduction zone earthquakes (e.g., Lay et al., 2012; Lay & Bilek, 2007). In the following, we will show that by extending these inelastic wedge deformation models to three dimensions (3-D), the variation of sediments and hence the variation of material strength in the Japan Trench margin can explain the puzzling along-arc variations of tsunamigenesis and near-trench slip observed in the 2011 Tohoku earthquake.

2. 3-D Dynamic Rupture Model With Inelastic Wedge Deformation

We consider a 10°-dipping subduction plate interface underlying a homogeneous sedimentary wedge with surface slope 5° and backstop thickness 15 km (Figure 1a). The fault is 57.735 km along dip and 240 km along strike. The material properties in the wedge are $\rho = 2{,}500$ kg/m^3, $V_P = 3{,}464$ m/s, and $V_S = 2{,}000$ m/s, where ρ is density, V_P is P wave speed, and V_S is S wave speed. The material properties outside the wedge are everywhere $\rho' = 2{,}500$ kg/m^3, $V_P' = 6{,}000$ m/s, and $V_S' = 3{,}464$ m/s. This simple crustal structure includes a compliant sedimentary wedge (shear modulus is 10 GPa vs. 30 GPa outside the wedge) but ignores other heterogeneities that are important in affecting wave propagation. The velocity heterogeneities may have only second-order effects on inelastic deformation, which will be incorporated in a future study. A compliant sedimentary wedge can interact constructively with the free surface to significantly enhance the slip at trench and hanging wall ground motion (e.g., Lotto et al., 2017; Ma & Beroza, 2008). Wedge compliance can also lead to slow rupture velocity (Lotto et al., 2017). The fault in our model is confined to the upper 15 km; therefore, this is not a Tohoku earthquake model but a model aiming to capture important rupture characteristics in the upper 10–15 km of the Tohoku earthquake that may be general to many other subduction zone earthquakes (e.g., Lay et al., 2012). Our fault dimensions and geometry are similar to the model of Tanioka and Seno (2001) for the 1896 Sanriku earthquake.

The absolute stress conditions are required to model inelastic deformation. Here we adopt the analytical solution for a noncohesive Coulomb wedge (Dahlen, 1984) to specify the initial stress conditions in the wedge:

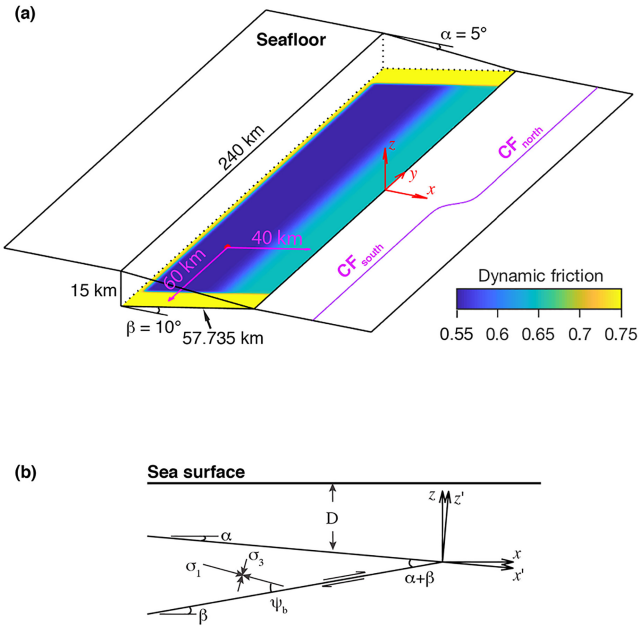

Figure 1. (a) Model geometry. The red dot denotes the hypocenter. The color shows the distribution of dynamic friction on the fault. Together with fluid overpressure, the effective friction on the fault is small (see text for details). The dynamic friction increases smoothly to a larger value (0.65) to induce negative stress drop within ~20 km from the trench. Similar tapering is also seen on three other edges of the fault to stop rupture smoothly. The rupture length with positive stress drop is ~210 km. The magenta curve on the right shows a schematic variation of closeness-to-failure (CF) of wedge from south to north. (b) A schematic cross section of the model geometry. The angle between the maximum compressive stress σ_1, and the fault is denoted by ψ_b. CF = closeness-to-failure.

$$\begin{aligned}\sigma^*_{z'z'} &= (1-\lambda)pgz' \cos\alpha,\\ \sigma_{x'z'} &= -(\rho-\rho_w)gz' \sin\alpha,\end{aligned} \tag{1}$$

where the sign convention of continuum mechanics is used, the superscript * denotes effective stress, the axes x' and z' and surface slope α are shown in Figure 1b, g is gravity, λ is the pore pressure ratio in the wedge ($\lambda = \frac{p_f - \rho_w gD}{-\sigma_{z'z'} - \rho_w gD}$), p_f is pore fluid pressure, ρ_w is water density, and D is ocean depth. The stress $\sigma^*_{x'x'}$ can be calculated from the Mohr-Coulomb failure criterion and equation (1) by assuming a critical wedge. All the stresses are linearly depth dependent.

We specify the angle between the maximum compressive stress and the basal fault as $\psi_b = 20°$, which is consistent with focal mechanisms of small earthquakes in the Japan Trench margin at this depth range (Hardebeck, 2012). This angle along with an assumed basal friction $\mu_b = 0.6$ (Byerlee, 1978) directly determines $\lambda = 0.7423$ (fluid overpressure) and the internal friction of the wedge $\mu = 0.6488$ in the solution of Dahlen (1984). To extend the stress to 3-D, we assume that $\sigma^*_{y'y'} = 0.5\left(\sigma^*_{x'x'} + \sigma^*_{z'z}\right)$ and $\sigma_{x'y'} = \sigma_{y'z'} = 0$, which implies that the maximum compressive stress is perpendicular to the fault strike and can be easily changed in other stress environments. Note that these stress conditions drive a noncohesive wedge on the verge of failure; we will add cohesion later to set the wedge in a noncritical state initially.

The Drucker-Prager yield criterion (Drucker & Prager, 1952) is used to model yielding in the wedge

$$\sqrt{\frac{1}{2}s_{ij}s_{ij}} \le c\cos\phi - \frac{\sigma^*_{kk}}{3}\sin\phi, \tag{2}$$

where the summation over repeated indices is implied, s_{ij} is the deviatoric stress tensor, c is cohesion, and ϕ is internal friction angle (i.e., $\phi = tan^{-1}\mu$). The pressure dependence of yield strength in this criterion can significantly enhance inelastic failure at shallow depths because of the low confining pressure, forming a "flower-like" damage zone (e.g., Kaneko & Fialko, 2011; Ma, 2008; Ma & Andrews, 2010; Roten et al., 2017; Wollherr et al., 2019). We consider undrained material response with Skemption's coefficient 0.6 and Biot's coefficient 0.5. Dynamic pore pressure change during earthquake rupture is also considered (Viesca et al., 2008). Yielding is allowed in shear only, with no inelastic dilatancy or compaction (e.g., Andrews, 2005).

We define an initial closeness-to-failure (CF) parameter

$$CF = \sqrt{\frac{1}{2}s^0_{ij}s^0_{ij}} \Big/ \left(c\cos\phi - \frac{\sigma^{*,0}_{kk}}{3}\sin\phi\right), \tag{3}$$

where the superscript 0 denotes the initial state. The CF is thus between 0 (far from failure) and 1 (on the verge of failure). In the following, we determine wedge cohesion by the assumed CF parameter from equation (3).

To consider the variation of sediments in the Japan Trench margin, we vary the cohesion along strike. The variation of wave speeds is not included in this study to keep the models simple. Because of the low shear strength of sediments, we set the CF higher in the north, implying lower cohesion and closer to failure initially. The CF is constant at each cross section (i.e., independent of x and z). We specify $CF_{\text{south}} = 0.7$ and $CF_{\text{north}} = 0.95$ and allow the CF to transition smoothly along strike (y axis) as $CF(x,y,z) = \frac{CF_{\text{north}}+CF_{\text{south}}}{2} + \frac{CF_{\text{north}}-CF_{\text{south}}}{2}\tanh\left(\frac{y}{5}\right)$, where y is in kilometers (Figure 1a). The CF thus specified transitions from 0.7 (south) to 0.95 (north) over about 20 km around $y = 0$. The determined cohesion at each cross section

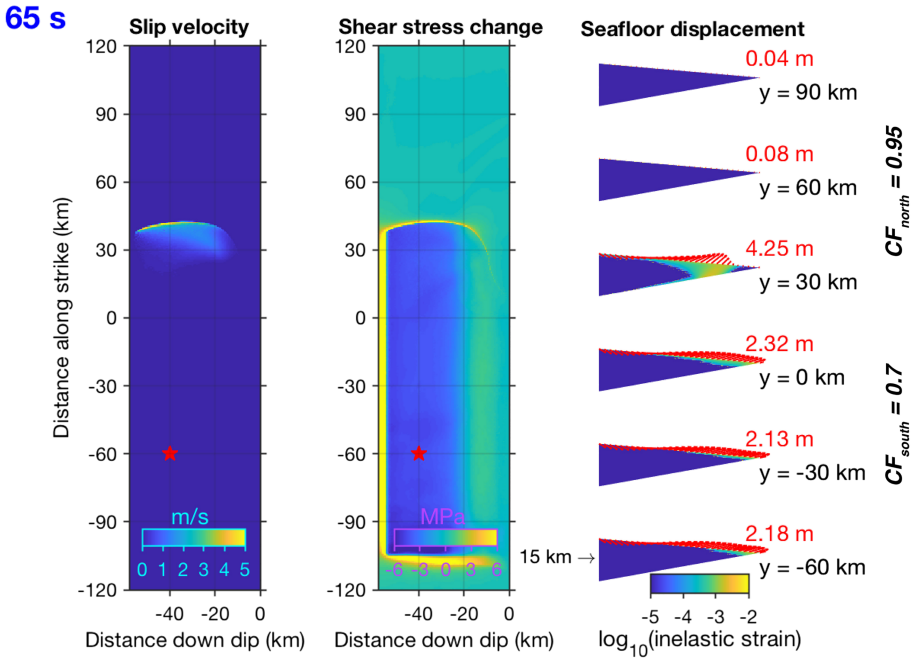

Figure 2. Snapshots of slip velocity and shear stress change (both are along-dip component) are mapped on the fault at 65 s. Seafloor displacements (red arrows; and red numbers denoting peak uplift) and inelastic shear strain (equivalent to volume density of seismic potency) at the same time are shown in six cross sections on the right. The along-strike distance is denoted on the lower right of each cross section. The rupture is pulse-like due to a narrow fault width compared to its length. Shear stress drops in the deeper section of the fault while in the upper 20 km increases due to the dynamic friction shown in Figure 1a. As the rupture propagates to the north into the high *CF* region (e.g., $y = 30$ km), large inelastic strain develops in the wedge, causing larger seafloor uplift than the south without near-trench slip. Seafloor displacements in the south are mostly parallel to the fault while in the north more vertical due to inelastic deformation. CF = closeness-to-failure.

increases linearly with depth as the initial stress field is linear with depth. We will see that this variation of *CF* (hence cohesion) alone can give rise to the along-strike variations of tsunami generation observed in the 2011 Tohoku earthquake.

A simple time-weakening friction law is used to model dynamic rupture on the fault (Andrews, 2004). The friction coefficient drops linearly from static friction μ_s to dynamic friction μ_d over a characteristic time t_c once slip initiates. This friction law is similar to the slip-weakening friction law (Andrews, 1976), except that the characteristic slip-weakening distance (D_c) is variable on the fault to ensure that the breakdown zone is well resolved. At rupture front, stress drops as abruptly as a numerical scheme allows, and friction is rate independent.

The initial shear and effective normal stresses on the fault can be calculated from the initial stress conditions at the bottom of wedge, which also increase linearly with depth. We assume no abrupt pore pressure change across the fault. The initial basal friction is $\mu_b = 0.6$ (specified previously). Note along with $\lambda = 0.7423$ (fluid overpressure), the effective friction on the fault is only $(1-\lambda)\mu_b = 0.1546$. We assume static friction $\mu_s = 0.75$ and dynamic friction $\mu_d = 0.55$; thus, the dynamic stress drop is 5% of the initial effective normal stress on the fault. The S ratio (Andrews, 1976), $S = \frac{\mu_s - \mu_b}{\mu_b - \mu_d}$, is equal to 3, to prevent supershear rupture on the fault. In the upper ~20 km of the fault plane (corresponding to upper ~3.47 km along depth from trench), we smoothly increase dynamic friction μ_d to 0.65 (Figure 1a) to induce negative stress drops, mimicking velocity-strengthening friction. Similar tapering is done on the other three edges of the fault to smoothly stop the rupture. The characteristic weakening time is $t_c = 0.375$ s, corresponding to the time for S wave to propagate ~3 elements on the fault (described below). The hypocenter is located 40 km down dip from the trench and 60 km north of the southern fault boundary. To nucleate the rupture, we force the rupture to spread at 1,000 m/s initially from the hypocenter until it propagates spontaneously shortly afterward.

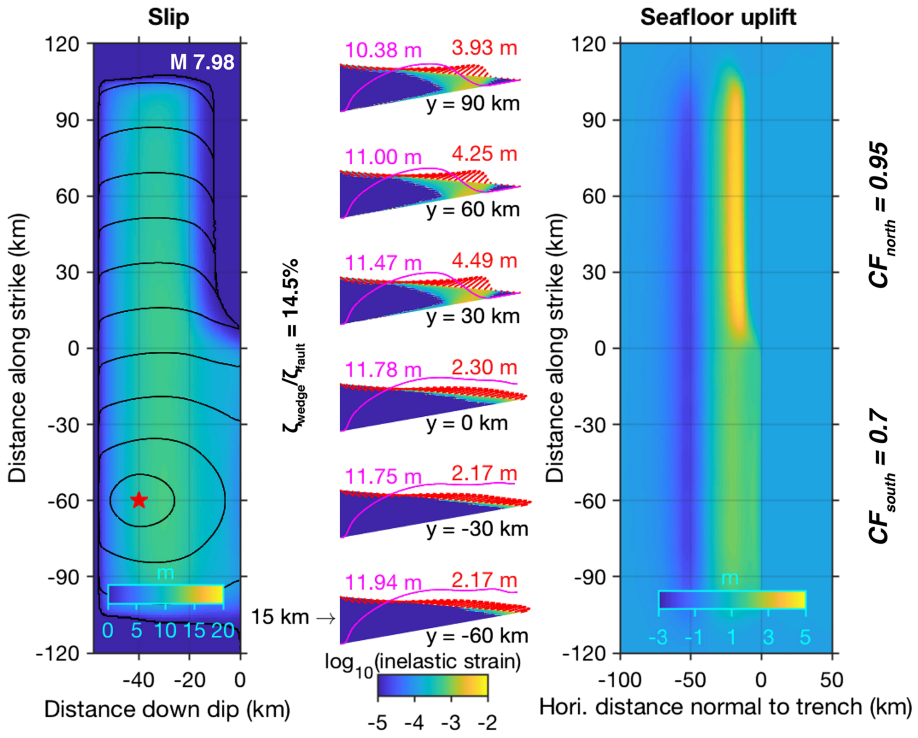

Figure 3. Distribution of slip on fault, final seafloor displacement (red arrows), on-fault slip (magenta curves), and inelastic shear strain (in logarithmic scale) at six cross sections, and surface map of final seafloor uplift are shown for the case of $CF_{\text{south}} = 0.7$ and $CF_{\text{north}} = 0.95$. Rupture time contours every 10 s, and moment magnitude are shown in the left panel. The rupture velocity along strike is ~1.8 km/s. The seismic potency ratio is shown between the first two panels. The red and magenta numbers in the middle panel denote the peak seafloor uplift and peak fault slip, respectively, at each cross section. The large inelastic strain to the north significantly decreases fault slip near the trench and increases seafloor uplift, resulting in a narrow strip of seafloor uplift that can excite efficiently dispersive tsunami waves. The along-strike variations of seafloor uplift and fault slip near the trench are consistent with the observations in the 2011 Tohoku earthquake. CF = closeness-to-failure.

We use a finite-element method (e.g., Ma & Andrews, 2010) to model rupture dynamics, inelastic deformation, and associated seismic radiation. Our unstructured finite element mesh consists of about 320 million four-node tetrahedral elements. The element size is about 250 m around the wedge and fault and coarsens gradually to 10 km at a distance of ~1,000 km. The model boundary this far is to prevent contaminations from wave reflections off the boundaries and ensure an accurate static field once the waves propagate out of the region of interest. The unstructured mesh significantly reduces the number of degrees of freedom in the simulations. All the simulations are carried out to 200 s with a time step of 0.003125 s.

3. Results

We show the evolutions of slip velocity, shear stress change on fault, inelastic shear strain in the wedge, and seafloor displacements along six cross sections in Movie S1, with a snapshot shown in Figure 2. Initially, the rupture propagates at a slightly faster rupture velocity up dip (Mode II direction) than along strike (Mode III direction). Because the *CF* is low in the south, the wedge deforms nearly elastically (the inelastic deformation is only confined to very shallow depths). Although there is negative stress drop at shallow depths, the rupture breaks the trench energetically, generating large slip at the trench and nearly fault-parallel seafloor displacement, similar to elastic rupture models with the velocity-strengthening rate-and-state friction (e.g., Kozdon & Dunham, 2013). However, as the rupture propagates predominantly along strike to the north (with a rupture velocity ~1.8 km/s), the increase of *CF* gives rise to large inelastic deformation in the wedge, which generates more vertical seafloor displacement without near-trench slip. This is also shown in the final slip distribution and seafloor displacement (Figure 3). The peak uplift in

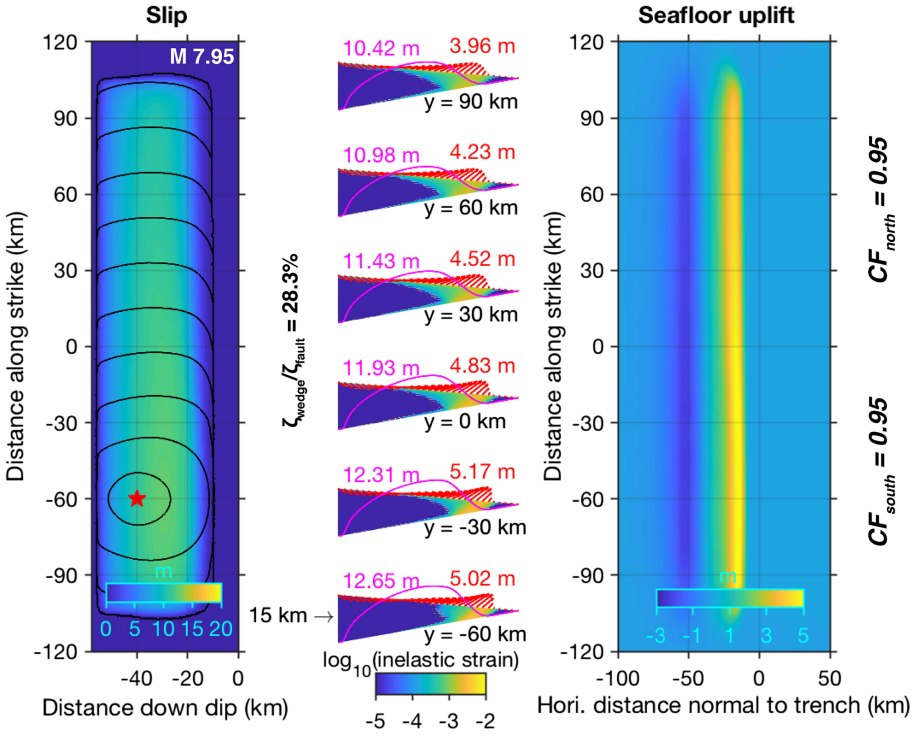

Figure 4. Same as Figure 3, except for $CF_{\text{south}} = 0.95$ and $CF_{\text{north}} = 0.95$. The inelastic wedge deformation is large along the entire fault length, causing peak uplift landward from the trench and diminished slip at the trench. The small wavelength seafloor uplift can generate highly dispersive tsunami waves to impact greatly on the rugged coasts of Sanriku. The seafloor uplift and slip pattern of this model may apply to the 1896 Sanriku earthquake. CF = closeness-to-failure.

the north is about twice as large as in the south; however, large trench slip occurs in the south. Inelastic strain shown here is equivalent to the volume density of seismic potency (Backus & Mulcahy, 1976). In this scenario, the potency release (ζ) in the wedge is 14.5% of that on fault. The total seismic moment is 1.18×10^{21} Nm, corresponding to M7.98. These results are consistent with the overall patterns of slip and tsunami heights in the Tohoku earthquake. Large slip (~50 m) were observed updip from the hypocenter at the trench in the bathymetry data (Fujiwara et al., 2011) and inferred from most inverse models. However, the tsunami heights were at least twice as large in the north (the Sanriku coast) than the south, but no large slip were observed at the trench in the north (Fujiwara et al., 2017). Again, our work here is not to model the 2011 Tohoku earthquake but to show that inelastic wedge deformation can explain the puzzling along-strike variations of seafloor uplift and near-trench slip observed in this earthquake.

A pronounced narrow strip of seafloor uplift from inelastic wedge deformation in the north is clearly seen in Figure 3. Such short-wavelength inelastic uplift, compared to the broader elastic uplift by large near-trench slip in the south, can excite more dispersive tsunami waves, which were also observed offshore the Sanriku region in the 2011 Tohoku earthquake (e.g., Tappin et al., 2014). These short-wavelength dispersive tsunami waves can interact efficiently with the rugged coasts of Sanriku (consisting of various small wavelengths) to amplify tsunami inundation and runup. A narrow strip of initial sea surface displacement extending ~39–40°N was also obtained by the inversion of tsunami data in the Tohoku earthquake (e.g., Dettmer et al., 2016), which is consistent with our results in the north. Their narrow initial sea surface heights, however, span over both seaward and landward sides of the trench, which may be due to a resolution issue.

As the *CF* in the north decreases, the inelastic wedge deformation reduces (Figures S2–S4), as expected. However, clear differences between north and south can still be seen if there is a difference in *CF*. The ratio of seismic potency, $\frac{\zeta_{\text{wedge}}}{\zeta_{\text{fault}}}$, reduces to 9.7% ($CF_{\text{north}} = 0.9$), 7.4% ($CF_{\text{north}} = 0.85$), and 5.3% ($CF_{\text{north}} = 0.7$), respectively, but the seismic moment increases slightly because elastic deformation requires more slip on the fault. In the case of $CF_{\text{north}} = CF_{\text{south}} = 0.7$, large trench slip causes large horizontal seafloor

displacement along the entire fault, which is close to an elastic case. When the *CF* is large across the entire region ($CF_{north} = CF_{south} = 0.9$ and $CF_{north} = CF_{south} = 0.95$; Figures S5 and 4), we see large seafloor uplift landward from the trench without trench slip along the entire fault length. The ratio of seismic potency is the largest (28.3%) for $CF_{north} = CF_{south} = 0.95$. This case has also the minimum moment but the largest seafloor uplift. We suggest that the overall patterns of seafloor uplift and slip in this case may apply to the 1896 Sanriku earthquake due to the large amounts of sediments in the entire source region.

4. Discussion and Conclusions

Our simple 3-D dynamic rupture models for a M8 shallow subduction zone earthquake show that inelastic wedge deformation along with along-arc variation of sediment thickness can give rise to important along-arc variations of seafloor uplift and near-trench slip in the Japan Trench margin. In the northern margin where large amounts of sediments are present, coseismic failure of wedge sediments can induce large seafloor uplift landward from the trench while reducing near-trench slip. In the south where sediments are scarce, the wedge deforms nearly elastically, giving rise to large slip at the trench, nearly horizontal seafloor displacement, but small seafloor uplift due to a shallow fault dip. The overall patterns of seafloor uplift and fault slip at the trench from our models are consistent with the observations of tsunami heights (Mori et al., 2011) and bathymetric data before and after the Tohoku earthquake (Fujiwara et al., 2011, 2017). Therefore, we conclude that the large tsunami heights in the Sanriku coast by the 2011 Tohoku earthquake are likely due to inelastic wedge deformation, not large slip at the trench. This is at least a plausible and satisfactory explanation to the puzzling observations of the 2011 Tohoku earthquake. The possibility of a large submarine landslide or large near-trench slip in the north is ruled out by the bathymetry data (Fujiwara et al., 2017). We also suggest that the large tsunami from the 1896 Sanriku earthquake could be due to inelastic wedge deformation (see Figure 4).

Sediments that undergo changes under various pressure and temperature conditions have long been realized to contribute greatly to the complexities of subduction zone earthquakes (e.g., Dixon & Moore, 2007; Ruff, 1989). In understanding earthquake mechanics, sediment effects have mostly been confined to the framework of elastic dislocation theory. For example, low rigidity of sediments can increase slip and seafloor deformation while the moment is kept constant, and can lead to slow rupture velocity (e.g., Lay & Bilek, 2007; Polet & Kanamori, 2000; Satake & Tanioka, 1999). However, the elastic theory ignores the low strength of sediments and thus inelastic deformation, which is well recognized in many other fields. Elastic dislocation models can face challenges in explaining critically important observations such as the ones being addressed here. Similar challenges arise in explaining tsunamigenesis when the dip of subduction megathrusts is very shallow, such as 2.0–5.0° for the 2010 Mentawai tsunami earthquake and 2.5–7.5° for the 2018 Hawaii thrust earthquake (Lay et al., 2018). These thinly tapered sedimentary wedges, however, can promote inelastic deformation because dynamic stress concentration in the wedge can be large.

Significant inelastic off-fault deformation has recently been documented for continental earthquakes (e.g., Dolan & Haravitch, 2014; Milliner et al., 2015; Rockwell et al., 2002; Zinke et al., 2014, 2019). Dynamic rupture models (e.g., Kaneko & Fialko, 2011; Roten et al., 2017; Wollherr et al., 2019) showed that inelastic off-fault deformation reduces fault slip at shallow depths, consistent with our subduction zone model results, which can explain the shallow slip deficit of earthquakes inferred from geodetic data (e.g., Fialko et al., 2005). We suggest that if shallow slip deficit is significant on continents, it is likely more significant in shallow subduction zones, due to low strength of marine sediments and possible high pore fluid pressure (e.g., Saffer & Tobin, 2011) in enhancing inelastic deformation. Shallow slip deficit, efficient tsunamigenesis, and anomalous energy radiation in shallow subduction zones can potentially all be closely related to inelastic deformation of sediments (Ma & Hirakawa, 2013).

The northern Japan Trench margin is geologically nonaccretionary (e.g., Tsuru et al., 2002) although the amount of sediments in the Sanriku section is large. The inelastic deformation of sediments can be important in most accretionary subduction zones, such as Alaska, Sumatra, Cascadia, Nankai, Hikurangi, and southern Chile, where great tsunamigenic megathrust earthquakes do occur. The prevailing elastic dislocation models, ignoring inelastic wedge deformation, may overestimate the near-trench slip and misinterpret the physics of tsunamigenesis. The seismic, ocean acoustic, and tsunami signals from these inelastic

wedge deformation models are likely different from those of elastic dislocation models, which can play important roles in tsunami early warning (e.g., Kozdon & Dunham, 2014). It is urgent to examine these signals to further validate and improve the earthquake rupture models.

Acknowledgments
S. M. is especially grateful to Tetsuzo Seno for the suggestion on looking at the sediment variation along the Japan Trench and to Nobuki Kame for hosting his sabbatical leave at the Earthquake Research Institute of the University of Tokyo, where the idea of this work was come up with. Eric Dunham and Alice-Agnes Gabriel provided constructive reviews that greatly improved the manuscript. This work is supported by the National Science Foundation (Award 1620201). All the simulations were carried out at the Center for High-Performance Computing of the University of Southern California. All the data reported in this work can be found in this paper and the references.

References

Andrews, D. J. (1976). Rupture velocity of plane strain shear cracks. *Journal of Geophysical Research*, *81*(32), 5679–5687. https://doi.org/10.1029/JB081i032p05679

Andrews, D. J. (2004). Rupture models with dynamically determined breakdown displacement. *Bulletin of the Seismological Society of America*, *94*(3), 769–775. https://doi.org/10.1785/0120030142

Andrews, D. J. (2005). Rupture dynamics with energy loss outside the slip zone. *Journal of Geophysical Research*, *110*, B01307. https://doi.org/10.1029/2004JB003191

Backus, G., & Mulcahy, M. (1976). Moment tensors and other phenomenological descriptions of seismic sources. I. Continuous displacements. *Geophysical Journal of the Royal Astronomical Society*, *46*(2), 341–361. https://doi.org/10.1111/j.1365-246X.1976.tb04162.x

Byerlee, J. (1978). Friction of rocks. *Pure and Applied Geophysics*, *116*(4-5), 615–626. https://doi.org/10.1007/BF00876528

Dahlen, F. A. (1984). Noncohesive critical Coulomb wedges: An exact solution. *Journal of Geophysical Research*, *89*(B12), 10125–10133. https://doi.org/10.1029/JB089iB12p10125

Dettmer, J., Hawkins, R., Cummins, P. R., Hossen, J., Sambridge, M., Hino, R., & Inazu, D. (2016). Tsunami source uncertainty estimation: The 2011 Japan tsunami. *Journal of Geophysical Research: Solid Earth*, *121*, 4483–4505. https://doi.org/10.1002/2051JB012764

Dixon, T. H., & Moore, J. C. (2007). The seismogenic zone of subduction thrust faults: Introduction. In D. H. Dixon & J. C. Moore (Eds.), *The Seismogenic Zone of Subduction Thrust Faults* (pp. 2–14). New York: Columbia University Press.

Dolan, J. F., & Haravitch, B. D. (2014). How well do surface slip measurements track slip at depth in large strike-slip earthquakes? The importance of fault structural maturity in controlling on fault slip versus off-fault surface deformation. *Earth and Planetary Science Letters*, *388*, 38–47. https://doi.org/10.1016/j.epsl.2013.11.043

Drucker, D. C., & Prager, W. (1952). Soil mechanics and plastic analysis or limit design. *Quarterly of Applied Mathematics*, *10*(2), 157–165. https://doi.org/10.1090/qam/48291

Fialko, Y., Sandwell, D., Simons, M., & Rosen, P. (2005). Three-dimensional deformation caused by the Bam, Iran, earthquake and the origin of shallow slip deficit. *Nature*, *435*(7040), 295–299. https://doi.org/10.1038/nature03425

Fujiwara, T., Ferreira, C. D. S., Bachmann, A. K., Strasser, M., Wefer, G., Sun, T., et al. (2017). Seafloor displacement after the 2011 Tohoku-oki earthquake in the northern Japan Trench examined by repeated bathymetric surveys. *Geophysical Research Letters*, *44*, 11,833–11,839. https://doi.org/10.1002/2017GL075839

Fujiwara, T., Kodaira, S., No, T., Kaiho, Y., Takahashi, N., & Kaneda, Y. (2011). The 2011 Tohoku-Oki earthquake: Displacement reaching the trench axis. *Science*, *334*(6060), 1240. https://doi.org/10.1126/science.1211554

Hardebeck, J. L. (2012). Coseismic and postseismic stress rotations due to great subduction zone earthquakes. *Geophysical Research Letters*, *39*, L21313. https://doi.org/10.1029/2012GL053438

Kanamori, H. (1972). Mechanism of tsunami earthquakes. *Physics of the Earth and Planetary Interiors*, *6*(5), 346–359. https://doi.org/10.1016/0031-9201(72)90058-1

Kaneko, Y., & Fialko, Y. (2011). Shallow slip deficit due to large strike-slip earthquakes in dynamic rupture simulations with elasto-plastic off-fault response. *Geophysical Journal International*, *186*(3), 1389–1403. https://doi.org/10.1111/j.1365-246X.2011.05117.x

Kozdon, J. E., & Dunham, E. M. (2013). Rupture to the trench: Dynamic rupture simulations of the 11 March 2011 Tohoku earthquake. *Bulletin of the Seismological Society of America*, *103*(2B), 1275–1289. https://doi.org/10.1785/0120120136

Kozdon, J. E., & Dunham, E. M. (2014). Constraining shallow slip and tsunami excitation in megathrust ruptures using seismic and ocean acoustic waves recorded on ocean-bottom sensor networks. *Earth and Planetary Science Letters*, *396*, 56–65. https://doi.org/10.1016/j.epsl.2014.04.001

Lay, T. (2018). A review of the rupture characteristics of the 2011 Tohoku-oki M_W 9.1 earthquake. *Tectonophysics*, *733*, 4–36. https://doi.org/10.1016/j.tecto.2017.09.022

Lay, T., & Bilek, S. (2007). Anomalous earthquake ruptures at shallow depths on subduction zone megathrusts. In D. H. Dixon & J. C. Moore (Eds.), *The Seismogenic Zone of Subduction Thrust Faults* (pp. 476–511). New York: Columbia University Press.

Lay, T., Ye, L., Kanamori, H., & Satake, K. (2018). Constraining the dip of shallow, shallowly dipping thrust events using long-period Love wave radiation patterns: Applications to the 25 October 2010 Mentawai, Indonesia, and 4 May 2018 Hawaii Island earthquakes. *Geophysical Research Letters*, *45*, 10,342–10,349. https://doi.org/10.1029/2018GL080042

Lay, T. H., Kanamori, C. A., Ammon, K. D., Koper, A. R., Hutko, L., Ye, H., et al. (2012). Depth-varying rupture properties of subduction zone megathrust faults. *Journal of Geophysical Research*, *117*, B04311. https://doi.org/10.1029/2011JB009133

Lotto, G. C., Dunham, E. M., Jeppson, T. N., & Tobin, H. J. (2017). The effect of compliant prisms on subduction zone earthquakes and tsunamis. *Earth and Planetary Science Letters*, *458*, 213–222. https://doi.org/10.1016/j.epsl.2016.10.050

Ma, S. (2008). A physical model for widespread near-surface and fault zone damage induced by earthquakes. *Geochemistry, Geophysics, Geosystems*, *9*, Q11009. https://doi.org/10.1029/2008GC002231

Ma, S. (2012). A self-consistent mechanism for slow dynamic deformation and tsunami generation for earthquakes in the shallow subduction zone. *Geophysical Research Letters*, *39*, L11310. https://doi.org/10.1029/2012GL051854

Ma, S., & Andrews, D. J. (2010). Inelastic off-fault response and three-dimensional earthquake rupture dynamics on a strike-slip fault. *Journal of Geophysical Research*, *115*, B04304. https://doi.org/10.1029/2009JB006382

Ma, S., & Beroza, G. C. (2008). Rupture dynamics on a bi-material interface for dipping faults. *Bulletin of the Seismological Society of America*, *98*(4), 1642–1658. https://doi.org/10.1785/0120070201

Ma, S., & Hirakawa, E. T. (2013). Dynamic wedge failure reveals anomalous energy radiation of shallow subduction earthquakes. *Earth and Planetary Science Letters*, *375*, 113–122. https://doi.org/10.1016/j.epsl.2013.05.016

Milliner, C. W. D., Dolan, J. F., Hollingsworth, J., Leprince, S., Ayoub, F., & Sammis, C. G. (2015). Quantifying near-field and off-fault deformation patterns of the 1992 Mw 7.3 Landers earthquake. *Geochemistry, Geophysics, Geosystems*, *16*, 1577–1598. https://doi.org/10.1002/2014GC005693

Mori, N., Takahashi, T., Yasuda, T., & Yanagisawa, H. (2011). Survey of 2011 Tohoku earthquake tsunami inundation and run-up. *Geophysical Research Letters*, *38*, L00G14. https://doi.org/10.1029/2011GL049210

Polet, J., & Kanamori, H. (2000). Shallow subduction zone earthquakes and their tsunamigenic potential. *Geophysical Journal International*, *142*(3), 684–702. https://doi.org/10.1046/j.1365-246x.2000.00205.x

Rockwell, T. K., Lindvall, S., Dawson, T., Langridge, R., Lettis, W. R., & Klinger, Y. (2002). Lateral offsets on surveyed cultural features resulting from the 1999 Izmit and Duzce Earthquakes, Turkey. *Bulletin of the Seismological Society of America*, *103*(2A), 629–640. https://doi.org/10.1785/0120120192

Roten, D., Olsen, K. B., & Day, S. M. (2017). Off-fault deformations and shallow slip deficit from dynamic rupture simulations with fault zone plasticity. *Geophysical Research Letters*, *44*, 7733–7742. https://doi.org/10.1002/2017GL074323

Ruff, L. J. (1989). Do trench sediments affect great earthquake occurrence in subduction zones? *Pure and Applied Geophysics*, *129*(1-2), 263–282. https://doi.org/10.1007/BF00874629

Saffer, D. M., & Tobin, H. J. (2011). Hydrogeology and mechanics of subduction zone forearcs: Fluid flow and pore pressure. *Annual Review of Earth and Planetary Sciences*, *39*(1), 157–186. https://doi.org/10.1146/annurev-earth-040610-133408

Satake, K., Fujii, Y., Harada, T., & Namegaya, Y. (2013). Time and space distribution of coseismic slip of the 2011 Tohoku earthquake as inferred from tsunami waveform data. *Bulletin of the Seismological Society of America*, *103*(2B), 1473–1492. https://doi.org/10.1785/0120120122

Satake, K., & Tanioka, Y. (1999). Sources of tsunami and tsunamigenic earthquakes in subduction zones. *Pure and Applied Geophysics*, *154*(3-4), 467–483. https://doi.org/10.1007/s000240050240

Seno, T. (2000). The 21 September, 1999 ChiChi earthquake in Taiwan: Implications for tsunami earthquakes. *Terrestrial, Atmospheric and Oceanic Sciences*, *11*(3), 701–708. https://doi.org/10.3319/TAO.2000.11.3.701(CCE)

Sun, T., Wang, K., Fujiwara, T., Kodaira, S., & He, J. (2017). Large fault slip peaking at trench in the 2011 Tohoku-oki earthquake. *Nature Communications*, *8*, 144044. https://doi.org/10.1038/ncomms14044

Tanioka, Y., & Satake, K. (1996). Tsunami generation by horizontal displacement of ocean bottom. *Geophysical Research Letters*, *23*(8), 861–864. https://doi.org/10.1029/96GL00736

Tanioka, Y., & Seno, T. (2001). The sediment effect on tsunami generation of the 1896 Sanriku tsunami earthquake. *Geophysical Research Letters*, *28*(17), 3389–3392. https://doi.org/10.1029/2001GL013149

Tappin, D. R., Grilli, S. T., Harris, J. C., Geller, R. J., Masterlark, T., Kirby, J. T., et al. (2014). Did submarine landslide contribute to the 2011 Tohoku tsunami? *Marine Geology*, *357*, 344–361. https://doi.org/10.1016/j.margeo.2014.09.043

Tsuru, T., Park, J.-O., Miura, S., Kodaira, S., Kido, Y., & Hayashi, T. (2002). Along-arc structural variation of the plate boundary at the Japan trench margin: Implication of interplate coupling. *Journal of Geophysical Research*, *107*(B12), 2357. https://doi.org/10.1029/2001JG0016664

Viesca, R. C., Templeton, E. L., & Rice, J. R. (2008). Off-fault plasticity and earthquake rupture dynamics, 2. Case of saturated off-fault materials. *Journal of Geophysical Research*, *113*, B09307. https://doi.org/10.1029/2007JB005530

Wang, K., & Hu, Y. (2006). Accretionary prisms in subduction zone cycles: The theory of dynamic Coulomb wedge. *Journal of Geophysical Research*, *111*, B06410. https://doi.org/10.1029/2005JB004094

Wollherr, S., Gabriel, A.-A., & Mai, P. M. (2019). Landers 1992 "reloaded": Integrative dynamic earthquake rupture modeling. *Journal of Geophysical Research: Solid Earth*, *124*. https://doi.org/10.1029/2018JB016355

Yamazaki, Y. K., Cheung, F., & Lay, T. (2018). A self-consistent fault slip model for the 2011 Tohoku earthquake and tsunami. *Journal of Geophysical Research: Solid Earth*, *123*, 1435–1458. https://doi.org/10.1002/2017JB014749

Zinke, R., Hollingsworth, J., & Dolan, J. F. (2014). Surface slip and off-fault deformation patterns in the 2013 Mw 7.7 Balochistan, Pakistan earthquake: Implications for controls on the distribution of near-surface coseismic slip. *Geochemistry, Geophysics, Geosystems*, *15*, 5034–5050. https://doi.org/10.1002/2014GC005538

Zinke, R., Hollingsworth, J., Dolan, J. F., & Dissen, R. V. (2019). Three-dimensional surface deformation in the 2016 Mw 7.8 Kaikoura, New Zealand, earthquake from optical image correlation: Implications for strain location and long-term evolution of the Pacific-Australian Plate boundary. *Geochemistry, Geophysics, Geosystems*, *20*, 1609–1628. https://doi.org/10.1029/2018GC007951